Robust retrieval of material chemical states in X-ray microspectroscopy

Ting Wang,[1] Xiaotong Wu,[1] Jizhou Li,[2,4] and Chao Wang[1,3,5]

[1]*Department of Statistics and Data Science, Southern University of Science and Technology, Shenzhen 518005, Guangdong Province, China*

[2]*School of Data Science, City University of Hong Kong, Hong Kong SAR, China*

[3]*National Centre for Applied Mathematics Shenzhen, Shenzhen 518055, Guangdong Province, China*

[4]*lijz@ieee.org*

[5]*wangc6@sustech.edu.cn*

Abstract: X-ray microspectroscopic techniques are essential for studying morphological and chemical changes in materials, providing high-resolution structural and spectroscopic information. However, its practical data analysis for reliably retrieving the chemical states remains a major obstacle to accelerating the fundamental understanding of materials in many research fields. In this work, we propose a novel data formulation model for X-ray microspectroscopy and develop a dedicated unmixing framework to solve this problem, which is robust to noise and spectral variability. Moreover, this framework is not limited to analyzing two-state material chemistry, making it an effective alternative to conventional and widely used methods. In addition, an alternative directional multiplier method with explicit or implicit regularization is applied to obtain the solution efficiently. Our framework can accurately identify and characterize chemical states in complex and heterogeneous samples, even under challenging conditions such as low signal-to-noise ratios and overlapping spectral features. By testing six simulated datasets, our method improves the existing methods by up to 151.84% and 136.33% in terms of the peak signal-to-noise ratio (PSNR) and the structural similarity index (SSIM) for the chemical phase map. Extensive experimental results on simulated and real datasets demonstrate its effectiveness and reliability.

1. Introduction

X-ray absorption spectroscopy (XAS) is a scientific technique that utilizes X-rays to investigate materials' electronic and structural properties. However, the spatial resolution of XAS is typically limited to the micron or sub-micron scale, which poses a challenge when studying materials with complex or heterogeneous structures. In recent years, spectroscopic full-field transmission X-ray microscopy (TXM) has emerged as a novel tool for nanoscale chemical imaging, with great potential in various multidisciplinary fields [1, 2]. By imaging at energy points across the absorption edge of the element of interest, TXM offers both high spatial resolution and chemical-specific information. Sub-50-nm resolution X-ray absorption near-edge structure (XANES) spectroscopy is routinely achieved with TXM-XANES, mainly operating in the hard X-ray regime (5 to 12 keV) [3–5]. Its application areas include materials science, physics, chemistry, and biology. For instance, it can be used for chemical mapping in battery studies [6,7] and mesoscale degradation [8].

In TXM-XANES, the intensity change of each pixel is scrutinized to generate XANES spectra that are matched against reference compounds. Some common techniques, including the edge-50 or linear combination fitting (LCF) [1], are used to fit the spectra, then a two-dimensional colormap is constructed to display the chemical phase combination of each pixel. The XANES Edge-50 point (energy at 0.5 spectrum position), which measures the absorption spectra of materials within the energy range of 5 keV to 12 keV, is a widely-used method defining the

absorption edge energy. The utilization of the Edge-50 XANES technique has been progressively examined for characterizing the chemical composition and structure of environmental material [9]. On the other hand, [10] proposed using LCF to determine the phase composition of a chemical sample from normalized XANES spectra. The XANES image at each pixel represents a spectrum at a particular location, which can be fitted with reference spectra to produce spatially resolved chemical state information. This technique significantly simplifies the processing and analysis of XANES spectra using LCF. These traditional methods have been extensively used in the literature [11–14]. Notably, Xiao et al. [15] present a workflow software integrating a few valuable tools for transmission X-ray microscopy data analysis, providing rich image visualization and processing routines.

Although traditional methods are widely applicable, they rely on high-quality TXM-XANES images. A relatively slow acquisition process is needed to achieve sufficient energy resolution, recording hundreds or thousands of energy points and a long exposure time. Fast TXM-XANES imaging is crucial for reliably solving morphological chemical phase transitions, as in 3D battery material research. To increase the speed of TXM-XANES imaging, energy points are reduced, or X-ray exposure time is minimized, which is more favorable for radiation-sensitive samples, similar to low-dose medical X-ray imaging applications. However, excessively short exposure times can result in measurements with strong noise [16]. Furthermore, when acquiring XANES data, there are many variations in the X-ray exposure conditions and inherent material properties, contributing to the variability of XANES spectra [17]. In the face of strong noise and spectral variability, the Edge-50 and LCT methods fail to obtain a reasonable interpretation of elemental and chemical information. Despite efforts to optimize microscope hardware, the physical limitations of the TXM-XANES imaging system remain challenging to overcome. To address this obstacle, computational algorithm development is inevitable for improving downstream analysis through fitting results.

Spectral unmixing methods [18] have numerous applications in imaging science, including remote sensing [19–21], optical microscopy [22], and X-ray imaging [23–25]. The unmixing technique aims to decompose a spectrum of mixed pixels into a set of distinct spectral signatures, known as endmembers, along with their corresponding fractional abundances [26, 27]. By utilizing spectral unmixing in X-ray microspectroscopy, the chemical states of materials can be directly obtained, bypassing the fitting process. Various regularizations have been developed in spectral unmixing methods to utilize the prior information on the abundance map against noise. In addition, in the face of spectral variability, many model formulations have been proposed in the unmixing problems [28–32]. The principle underlying the LCF method is essentially spectral unmixing [18], whereby the mixture is analyzed by determining the contribution of the reference spectra. However, it is sensitive to noise and limited in handling problems with spectral variability.

The TXM-XANES unmixing task involving spectral variability can be formulated as an optimization model. After extracting the scale factors from spectral variability in each pixel, the chemical map corresponding to different chemical states can be seen as a sequence of images. This allows us to utilize prior information and enhance the robustness of our model. In this study, we employ two regularization techniques to achieve this goal. Firstly, the explicit regularizer is applied to the reconstructed image to incorporate spatial and spectral information through pixel connections in the unmixing process [33, 34], an explicit regularizer pertains to prior information that is pre-defined in model-based methods. On the other hand, the Plug and Play (PnP) technique utilizes state-of-the-art denoisers to tackle linear inverse problems in various hyperspectral image processing tasks [35–41]. In contrast to traditional model-based methods, which require explicit and manually designed image priors, PnP can implicitly establish the prior information through the use of denoisers. Therefore, in the subsequent sections, we refer to PnP as an implicit regularizer. The main contributions of this paper are summarized as follows:
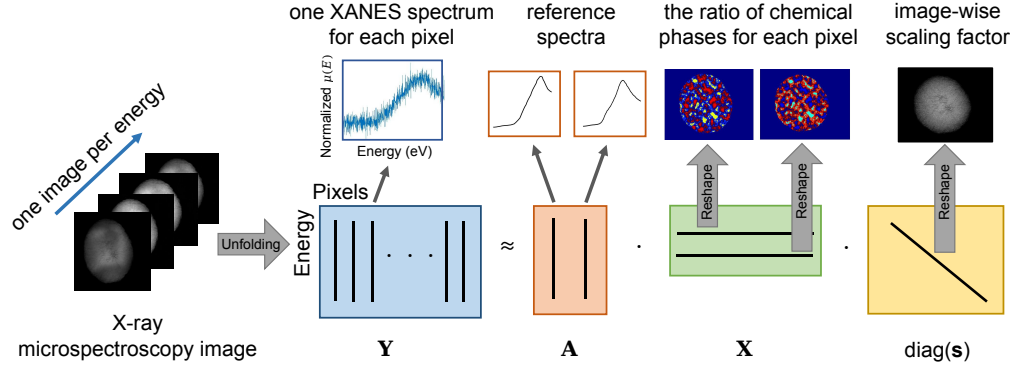
Fig. 1. Framework of the proposed model for material chemical states retrieval in the form of unmixing for X-ray microspectroscopy. The normalized XANES spectra from each pixel are unmixed to create a chemical phase map **X**, which also considers the image's scaling factor.

- We present a novel and robust framework for X-ray TXM-XANES imaging, which incorporates various realistic factors that affect the spectra, such as noise and spectral variability.

- Our proposed framework is evaluated extensively using both quantitative and qualitative methods on synthetic and experimental datasets. The results indicate that our proposed methods surpass the state-of-the-art. Our framework with an implicit regularization achieves the best performance.

The rest of the paper is organized as follows. In Section 2, we propose a novel data formulation model for the material chemical states retrieval in X-ray microspectroscopy and the corresponding algorithms to solve it. Section 3 presents the experimental results and subsequent discussions. Finally, Section 4 provides a summary and future perspectives.

2.   Proposed Robust Unmixing Framework

2.1.   Model Formulation

Here the observed XANES image is represented by $\mathbf{Y} = [\mathbf{y}_1, \mathbf{y}_2, \ldots, \mathbf{y}_N] \in \mathbb{R}^{T \times N}$, where each column vector is obtained by lexicographically ordering the TXM image with size $N = M \times K$, and T is the number of energy points. The LCF model generates the noisy measurements $\mathbf{Y}$ from the chemical phase map $\mathbf{M} = [\mathbf{m}_1, \mathbf{m}_2, \ldots, \mathbf{m}_n] \in \mathbb{R}^{L \times N}$, pixel-wisely.

$$\mathbf{y}_k = \mathbf{A}\mathbf{m}_k + \mathbf{r}_k, \ k = 1, \ldots, N, \tag{1}$$

where $\mathbf{A} \in \mathbb{R}^{T \times L}$ is the dictionary, representing spectra of the reference materials in the XANES images, L is the number of materials, and the noise $\mathbf{r}_k$ is assumed to follow Gaussian distribution.

Given $\mathbf{A} \in \mathbb{R}^{T \times L}$, LCF is to solve a least square problem. However, this is an inverse problem which is sensitive to the noise. In addition, the chemical phase map $\mathbf{m}_k$ is a vector with non-negative values but does not sum up to one. This is because of the illumination conditions and uncertainty in the chemical process. As a result, some critical prior information contained in $\mathbf{m}_k$ as an image is lost, and it becomes difficult to apply certain regularization techniques.

Here, we introduce the scaling factor s_k for this pixel-wise spectral variability such that this process can be effectively modeled by approximating the chemical phase map of each pixel with

the scaled version of the reference spectra. We split the $\mathbf{m}_k$ into two variables

$$\mathbf{m}_k = s_k \mathbf{x}_k,$$

where s_k is a scalar in the k-the pixel and $\mathbf{x}_k$ is the normalized chemical phase map which has
the sum-to-one property. Then the forward model (1) can be rewritten as

$$\mathbf{y}_k = s_k \mathbf{A} \mathbf{x}_k + \mathbf{r}_k, \ k = 1, \ldots, N, \tag{2}$$

In other words, we get the matrix form of (2) as

$$\mathbf{Y} = \mathbf{A} \mathbf{X} \mathrm{diag}(\mathbf{s}) + \mathbf{R}, \tag{3}$$

where $\mathrm{diag}(\mathbf{s})$ represents a diagonal matrix with its diagonal values $\mathbf{s} = [s_1, s_2, \ldots, s_N]^T$ and
$s_i \geq 0, \forall i \in 1, \ldots, N$. The noise term is $\mathbf{R} = [\mathbf{r}_1, \mathbf{r}_2, \ldots, \mathbf{r}_N]$. Fig. 1 gives the macro diagram
of spectral unmixing for the XANES imaging. With (3), we get an optimization problem:

$$\min_{\mathbf{X},\mathbf{s}} \quad \frac{1}{2} \|\mathbf{Y} - \mathbf{A} \mathbf{X} \mathrm{diag}(\mathbf{s})\|_F^2$$
$$\text{s.t.} \quad \mathbf{X} \geq \mathbf{0}, \ \mathbf{s} \geq \mathbf{0}, \ \mathbf{1}^T \mathbf{X} = \mathbf{1}, \tag{4}$$

where $\| \cdot \|_F$ is the Frobenius norm, i.e., $\|\mathbf{Z}\|_F = \sqrt{\sum z_{ij}^2}$ for any $\mathbf{Z}$. Note that combining $\mathbf{X}$
and $\mathbf{s}$ into a nonnegative least squares problem would lose some prior information on $\mathbf{X}$ itself,
especially when $\mathbf{X}$ and $\mathbf{s}$ are independent. In the following, we will utilize the prior information
and propose a robust optimization framework under a low exposure time measurement.

2.2. Explicit and Implicit Regularizations

Regularization is a widely-used technique in image processing to promote sparsity in terms of
certain transformations on the image [42, 43]. Here the normalized chemical phase map can be
regarded as a group of images and has a piece-wise spatial correlation. Hence, we first adapt
a regularization into (4) in a unified framework, and the proposed model can be expressed as
follows:

$$\min_{\mathbf{X},\mathbf{s}} \quad \frac{1}{2} \|\mathbf{Y} - \mathbf{A} \mathbf{X} \mathrm{diag}(\mathbf{s})\|_F^2 + \lambda \sum_{j=1}^{L} \Phi(\mathbf{x}_j) + I_{\Omega_1}(\mathbf{X}) + I_{\Omega_2}(\mathbf{s}), \tag{5}$$

where $\Phi(\mathbf{x})$ represents a regularization term enforcing prior knowledge of $\mathbf{x}$. The regularization
parameter is represented as λ. Here $\mathbf{x}_j$ is the j-th row in the chemical map $\mathbf{X}$, and I_Ω is the
indicator function for the nonnegative value, i.e.,

$$I_\Omega(\mathbf{x}) = \begin{cases} 0 & \mathbf{x} \in \Omega, \\ +\infty & \text{otherwise.} \end{cases} \tag{6}$$

In addition, $\Omega_1 = \{\mathbf{X} | \mathbf{X} \geq \mathbf{0} \text{ and } \mathbf{1}^T \mathbf{X} = \mathbf{1}\}$ and $\Omega_2 = \{\mathbf{s} | \mathbf{s} \geq \mathbf{0}\}$. Since the sparsity emerges in
terms of certain transformations, we define $\Phi(\mathbf{x}) = \phi_1 \circ \phi_2(\mathbf{x}) := \phi_1(\phi_2(\mathbf{x}))$ where ϕ_1 is the
sparse term and ϕ_2 is certain transformations. After splitting the variables, the problem in (6)
with auxiliary variables can be expressed as follows:

$$\min_{\mathbf{X},\mathbf{s}} \quad \frac{1}{2} \|\mathbf{Y} - \mathbf{A} \mathbf{M}\|_F^2 + \lambda \sum_{j=1}^{L} \phi_1(\mathbf{u}_j) + I_{\Omega_1}(\mathbf{W}) + I_{\Omega_2}(\mathbf{t})$$
$$\text{s.t.} \quad \mathbf{M} = \mathbf{X} \mathrm{diag}(\mathbf{s}), \mathbf{u}_j = \phi_2(\mathbf{x}_j), \mathbf{W} = \mathbf{X}, \mathbf{t} = \mathbf{s}. \tag{7}$$

and the augmented Lagrangian is as follows:

$$\mathcal{L}(\mathbf{X}, \mathbf{s}, \mathbf{M}, \mathbf{U}, \mathbf{W}, \mathbf{t}, \mathbf{F}) = \frac{1}{2}\|\mathbf{Y} - \mathbf{A}\mathbf{M}\|_F^2 + \lambda \sum_{j=1}^{L} \phi_1(\mathbf{u}_j) + \frac{\rho}{2}\|\mathbf{X}\text{diag}(\mathbf{s}) - \mathbf{M} + \mathbf{C}\|_F^2 - \frac{\rho}{2}\|\mathbf{C}\|_F^2$$

$$+ \frac{\rho}{2} \sum_{j=1}^{L} \|\phi_2(\mathbf{x}_j) - \mathbf{u}_j + \mathbf{d}_j\|_2^2 - \frac{\rho}{2}\|\mathbf{d}_j\|_2^2 + \frac{\rho}{2}\|\mathbf{X} - \mathbf{W} + \mathbf{E}\|_F^2 - \frac{\rho}{2}\|\mathbf{E}\|_F^2$$

$$+ \frac{\rho}{2}\|\mathbf{s} - \mathbf{t} + \mathbf{g}\|_2^2 - \frac{\rho}{2}\|\mathbf{g}\|_2^2,$$

(8)

where $\mathbf{C}, \mathbf{D} = [\mathbf{d}_1, \mathbf{d}_2, \ldots, \mathbf{d}_L]$, $\mathbf{E}, \mathbf{g}$ are dual variables and λ, ρ are positive parameters. Denote $\mathbf{F} = [\mathbf{C}; \mathbf{D}; \mathbf{E}; \text{diag}(\mathbf{g})]$. It's worth noting that λ regulates the influence of the regularization term and significantly affects the unmixing results, whereas ρ is a penalty parameter in the augmented Lagrangian function and only affects the convergence speed. Now, we present two types of regularizations for this unified framework (5).

Explicit Regularization. We first adapt some explicit regularization in the model (5). In order to promote sparsity prior to the XANES images, $\phi_1(\cdot)$ is denoted by $\|\cdot\|_1$. Here we consider the linear transformations ϕ_2 to project the image into another domain. Note that $\|\phi_2(\mathbf{x}_j)\|_1$ becomes total variation [44] if we choose $\phi_2(\cdot)$ as a discrete gradient operator. We apply the alternating direction method of multipliers (ADMM) [45] to solve this model. All these variables are updated alternatively, and the sub-problems' derivation has been included in the Supplement Material. Algorithm 1 summarizes the whole process for solving model (8) with explicit regularization. Moreover, we further the sequence generated by Algorithm 1, which has at least one accumulation point satisfying the Karush-Kuhn-Tucker (KKT) conditions [46] of (8) with explicit regularization. The proof can be found in Supplementary Material.

Implicit Regularization. Designing an explicit regularizer can be challenging, as complex regularizers often complicate optimization problems, making the entire process more difficult. Rather than using a handcrafted regularizer, we aim to implicitly leverage prior knowledge about the spectral characteristics of materials in the scene to achieve better regularized unmixing results. In the implicit regularization, $\phi_1(\cdot)$ enforces prior knowledge of $\mathbf{X}$, while $\phi_2(\cdot)$ represents identity transformation, i.e. $\phi_2(\mathbf{x}) = \mathbf{x}$. All these variables are updated sequentially, and the solution to the subproblem involving the variables $\mathbf{X}$ and $\mathbf{U}$, which differs from the explicit regularization, is thoroughly elucidated in the Supplementary Material. In the case of the subproblem $\mathbf{u}_j$, the $\mathbf{u}_j$-subproblem is to solve a proximal operator as follows:

$$\mathbf{u}_j^{k+1} = \arg\min_{\mathbf{u}} \frac{\rho}{2}\|\mathbf{u}_j - \mathbf{x}_j^{k+1} - \mathbf{d}_j^k\|_F^2 + \lambda\phi_1(\mathbf{u}_j). \quad (9)$$

We define $\sigma = \sqrt{\lambda/\rho}$, it is not difficult to show that (9) is

$$\mathbf{u}_j^{k+1} = \arg\min_{\mathbf{u}} \frac{1}{2\sigma^2}\|\mathbf{u}_j - \mathbf{x}_j^{k+1} - \mathbf{d}_j^k\|_F^2 + \phi_1(\mathbf{u}_j). \quad (10)$$

Treating as $\mathbf{x}_j^{k+1} + \mathbf{d}_j^k$ as the "noisy" image, (10) minimizes the residue between $\mathbf{x}_j^{k+1} + \mathbf{d}_j^k$ and the "clean" image $\mathbf{u}_j$ using the prior $\phi_1(\mathbf{u}_j)$, so (10) can be viewed as a standard image-denoising problem. We employ established and effective denoising operators in the PnP framework iterations, such as the conventional BM3D [47] or DnCNN [48], which utilizes deep learning. To adapt to the variation in noise during each iteration process. we increase $\rho^{k+1} = \gamma_k\rho^k$ for $\gamma_k \geq 1$, it has been used in various problem [49, 50]. Incorporating it into the (9), and define $\sigma^k = \sqrt{\lambda/\rho^k}$ is a parameter controlling the strength of the denoiser. After acquiring the necessary

denoising operators, we update the primal and dual variables in the ADMM process, following Algorithm 1.

Algorithm 1: The Framework for TXM-XANES Image Unmixing with Explicit Regularizer and Implicit Regularizer (denoted as RUM_{ex} and RUM_{im}, respectively).

Input: A TXM-XANES image $\mathbf{Y}$, Dictionary $\mathbf{A}$.
Output: Phase map $\mathbf{X}$, Scaling factor $\mathbf{s}$.

1: Initialize: $\mathbf{X}$ and $\mathbf{s}$ and choose parameter ρ, λ and γ.
2: **while** not converged or iterations are not reached **do**
3:     $\mathbf{X}$ is updated by
$$\begin{cases} ((\mathbf{M}-\mathbf{C})\mathrm{diag}(\mathbf{s}) + \sum_{j=1}^{L} \phi_2^T(\mathbf{u}_j - \mathbf{d}_j) + \mathbf{W} - \mathbf{E})(\mathrm{diag}(\mathbf{s})^2 - \Delta + \mathbf{I})^{-1} & \text{for } RUM_{ex}, \\ ((\mathbf{M}-\mathbf{C})\mathrm{diag}(\mathbf{s}) + \sum_{j=1}^{L} (\mathbf{u}_j - \mathbf{d}_j) + \mathbf{W} - \mathbf{E})(\mathrm{diag}(\mathbf{s})^2 + 2\mathbf{I})^{-1} & \text{for } RUM_{im}, \end{cases}$$
4:     Normalize $\mathbf{X}$ such that $\mathbf{1}^T\mathbf{X} = \mathbf{1}$,
5:     $\mathbf{s} \leftarrow (\mathbf{X}^T\mathbf{X}+\mathbf{I})^{-1}(\mathbf{X}^T(\mathbf{M}-\mathbf{C})+\mathbf{t}-\mathbf{g})$,
6:     $\mathbf{M} \leftarrow (\mathbf{A}^T\mathbf{A}+\rho\mathbf{I})^{-1}(\mathbf{A}^T\mathbf{Y}+\rho\mathbf{X}\mathrm{diag}(\mathbf{s})+\rho\mathbf{C})$,
7:     $\mathbf{U} \leftarrow \begin{cases} \mathbf{shrink}(\phi_2(\mathbf{x}_j)+\mathbf{d}_j, \frac{\lambda}{\rho}), & \text{for } RUM_{ex} \\ \mathbf{Denoiser}(\mathbf{x}_j + \mathbf{d}_j, \frac{\lambda}{\rho}), & \text{for } RUM_{im} \end{cases}$
8:     $\rho \leftarrow \gamma\rho$ for RUM_{im}
9:     $\mathbf{W} \leftarrow \max(\mathbf{X}+\mathbf{E}, \mathbf{0})$,
10:    $\mathbf{t} \leftarrow \max(\mathbf{s}+\mathbf{g}, \mathbf{0})$,
11:    $\mathbf{C} \leftarrow \mathbf{C}+\mathbf{X}\mathrm{diag}(\mathbf{s})-\mathbf{M}$,
12:    $\mathbf{d}_j \leftarrow \begin{cases} \mathbf{d}_j + \phi_2(\mathbf{x}_j) - \mathbf{u}_j, & \text{for } RUM_{ex} \\ \mathbf{d}_j + \mathbf{x}_j - \mathbf{u}_j, & \text{for } RUM_{im} \end{cases}$
13:    $\mathbf{E} \leftarrow \mathbf{E}+\mathbf{X}-\mathbf{W}$,
14:    $\mathbf{g} \leftarrow \mathbf{g}+\mathbf{s}-\mathbf{t}$.
15: **end while**

Remark 1 *Dictionary selection: The proposed algorithm can quickly and accurately extract the spectral signal from the XANES imaging data. However, the reference spectra are a critical component for achieving optimal performance. When the reference spectra are unknown, we use the conventional spectra extraction method, which is the vertex component analysis (VCA) [51] as a baseline for dictionary identification. In the real data analysis in Section 3.3, we demonstrate that using VCA with denoising results in more accurate reference spectra extraction, particularly in strong-noise environments.*

3. Experiments and Results

In this section, we will evaluate the performance of the proposed methods quantitatively and visually on both synthetic and actual datasets. Regarding the comparison with different priors, our methods are divided into two groups: the explicit regularization (RUM_{ex} denoted as total variation) and implicit regularization (RUM_{im} denotes as PnP with BM3D [47]). More results on different regularizers and the algorithm behaviors can be found in the Supplementary Material. These proposed methods will be assessed compared to the traditional methods, namely Edge-50 and LCF.

3.1. Experimental Settings and Evaluation Metrics

Data Description. The dataset presented in Fig. 2 comprises three X-ray projection images (Particles, Polymer, and Round) and three reconstructed slices (Wedge, Electrode, and Brine),
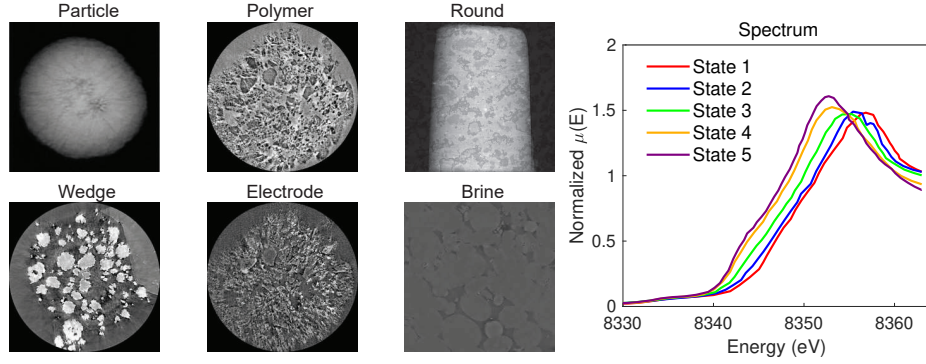
Fig. 2. Left: Typical examples of the test datasets: projections and reconstructed slices; Right: Normalized spectra under different Ni valence states of X-ray XANES in a battery cathode. State 1, 2, 3, 4, and 5 represent Ni's different valence states.

which are utilized to create a simulation of 2D and 3D TXM-XANES imaging scenarios. To generate simulated movie data, as shown in Fig. 2, the reference spectra of different Ni valence states are randomly assigned to pixels in the images for various phase maps. The sample is assumed to contain various valence states of Ni elements, and the proportion of Ni elements satisfies the sum-to-one constraint. We describe the state using number $(1, 2, 3, \ldots, L)$.

Evaluation Metrics. Each synthetic dataset frame is further corrupted with additive Gaussian noise with varying noise levels, with the standard deviation $\sigma \in [1, 7]$. For the performance assessment of the algorithms, we utilize two commonly used criteria to measure the accuracy of the phase map: the peak signal-to-noise ratio (PSNR) and the structural similarity index (SSIM). PSNR is defined as follows:

$$\text{PSNR} = 20 \times \log_{10} \left(\text{MAX/RMSE} \right), \tag{11}$$

where MAX is the maximum pixel value of the estimated image $\hat{\mathbf{X}}$ across all pixels, and RMSE is the root mean square error between $\hat{\mathbf{X}}$ and the ground truth $\mathbf{X}$. The RMSE is defined as:

$$\text{RMSE} = \sqrt{\frac{1}{n_1 n_2} \sum_{i=1}^{n_1} \sum_{l=1}^{n_2} \|\hat{x}(i, l) - x(i, l)\|^2}, \tag{12}$$

where n_1 and n_2 are the number of rows and columns in the image $\mathbf{X}$. We use the estimated phase map $\hat{\mathbf{X}}$ and the ground truth $\mathbf{X}$ to calculate PSNR. Then PSNR is calculated by the average of the PSNR of each chemical phase map.

SSIM is a metric that quantifies the similarity between two images, which is calculated by the average of the SSIM of each chemical phase map. The SSIM formula is expressed as follows:

$$\text{SSIM}(\hat{\mathbf{X}}, \mathbf{X}) = \frac{[(2\mu_{\hat{\mathbf{X}}}\mu_{\mathbf{X}} + c_1) * (2\sigma_{\hat{\mathbf{X}}\mathbf{X}} + c_2)]}{[(\mu_{\hat{\mathbf{X}}}^2 + \mu_{\mathbf{X}}^2 + c_1) * (\sigma_{\hat{\mathbf{X}}}^2 + \sigma_{\mathbf{X}}^2 + c_2)]}, \tag{13}$$

where $\mu_{\hat{\mathbf{X}}}$ and $\mu_{\mathbf{X}}$ represent the means of $\hat{\mathbf{X}}$ and $\mathbf{X}$, respectively. $\sigma_{\hat{\mathbf{X}}}$ and $\sigma_{\mathbf{X}}$ denote the standard deviations of $\hat{\mathbf{X}}$ and $\mathbf{X}$, respectively. $\sigma_{\hat{\mathbf{X}}\mathbf{X}}$ is the covariance of $\hat{\mathbf{X}}$ and $\mathbf{X}$, while c_1 and c_2 are small constants added to prevent division by zero errors and stabilize the formula.

3.2. Results of Synthetic Datasets

Different Noise Levels. In this simulation scenario, we assume that each of the six simulated movie image datasets exclusively contains two Ni elements, namely, state 1 and state 2 under
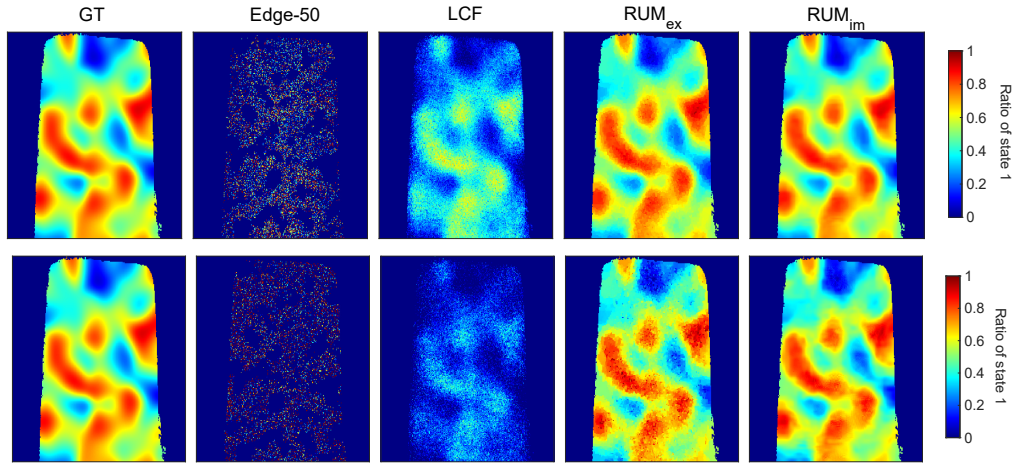
Fig. 3. A visual comparison of the chemical phase map for various methods on the Round data under different noise levels ($\sigma = 3$ on the top and $\sigma = 7$ on the bottom). Note that the other chemical map is the reverse since $L = 2$.

Table 1. Comparison of PSNR (dB) and SSIM in for six simulated datasets using different approaches and noise levels (σ is from 1 to 7).

Test set	σ	Edge-50		LCF		RUM$_{ex}$		RUM$_{im}$	
		PSNR	SSIM	PSNR	SSIM	PSNR	SSIM	PSNR	SSIM
Particle	1	8.98	0.10	16.11	0.57	38.22	0.94	**42.65**	**0.98**
	3	5.96	0.08	9.33	0.28	32.64	0.87	**37.36**	**0.96**
	5	5.73	0.07	6.80	0.22	29.59	0.76	**34.39**	**0.93**
	7	5.71	0.07	5.26	0.20	27.63	0.69	**31.39**	**0.87**
Electrode	1	9.19	0.23	17.37	0.51	42.39	0.95	**46.79**	**0.99**
	3	6.23	0.22	10.00	0.36	38.38	0.92	**42.27**	**0.98**
	5	6.01	0.22	7.29	0.35	33.65	0.83	**37.97**	**0.95**
	7	5.97	0.21	6.03	0.36	31.51	0.78	**35.21**	**0.92**
Polymer	1	11.20	0.23	19.94	0.59	42.36	0.95	**47.10**	**0.99**
	3	6.56	0.22	11.86	0.39	37.85	0.89	**42.74**	**0.98**
	5	6.07	0.21	8.94	0.35	32.44	0.75	**38.53**	**0.94**
	7	5.97	0.21	7.27	0.35	30.00	0.68	**34.29**	**0.86**
Wedge	1	10.04	0.23	19.23	0.56	47.26	0.99	**51.01**	**1.00**
	3	6.58	0.21	10.97	0.35	38.98	0.93	**43.35**	**0.99**
	5	6.23	0.21	8.15	0.34	33.65	0.83	**38.14**	**0.95**
	7	6.13	0.21	6.88	0.32	31.41	0.76	**34.86**	**0.89**
Round	1	7.06	0.04	12.17	0.50	35.28	0.92	**39.58**	**0.97**
	3	4.89	0.01	6.81	0.28	28.53	0.80	**34.14**	**0.94**
	5	4.66	0.01	5.06	0.22	26.35	0.70	**30.78**	**0.88**
	7	4.63	0.01	3.95	0.19	24.43	0.63	**28.19**	**0.80**
Brine	1	10.46	0.03	19.86	0.52	40.34	0.92	**45.40**	**0.97**
	3	4.96	0.01	10.54	0.24	35.59	0.83	**39.85**	**0.94**
	5	4.59	0.01	7.08	0.18	30.90	0.66	**37.01**	**0.91**
	7	4.55	0.01	5.17	0.17	28.52	0.56	**33.00**	**0.80**

different noise levels. This configuration results in a dictionary composed of two reference spectra. Consequently, the generated chemical maps illustrate the relative proportions of states 1 and 2, within the chemical material. To enhance clarity, when presenting these phase maps, each map distinctly portrays the proportion of one Ni element. This approach aligns with the constraint that the Ni element proportions collectively sum to one. In the case where $L = 2$, the second phase map showcases the inverse proportions of the elements. Table 1 displays the performance of both traditional methods and our proposed unmixing methods incorporating explicit and implicit regularizers with two reference spectra. The optimal results are highlighted in bold font. Overall, both of our methods outperform traditional techniques across all datasets. We observed approximately two times improvement in terms of PSNR compared to Edge-50, and about one time improvement compared to LCF. Our models exhibit remarkable robustness to a wide range of noise levels, particularly when the noise is substantial, as the chemical map is still reconstructed effectively. RUM_{im} improves RUM_{ex} by up to 2 dB in terms of PSNR and 0.1 in terms of SSIM under all noise conditions. However, the computational cost is much heavier than RUM_{ex}; See Supplementary Material. In Fig. 3, we compare the chemical phase maps of Round data obtained from various approaches under two kinds of noise levels. Except for Edge-50, we observe that the estimated phase maps are consistent with the ground truth (GT). However, under strong noise, our proposed methods yield less noisy phase maps closer to GT and preserve the image details. The Edge-50 and LCF methods are pixel-based and do not consider the spatial-spectral correlations in XANES images. Our proposed RUM_{ex} method employs fixed regularizers and lacks flexibility, while the PnP framework models priors using denoiser, thus eliminating the need for handcrafted regularizers.

Table 2. Comparison of PSNR (dB) and SSIM using different approaches with varying numbers of the reference spectra (the noise level σ is set as 3).

Test set	L	LCF		RUM_{ex}		RUM_{im}	
		PSNR	SSIM	PSNR	SSIM	PSNR	SSIM
Particle	3	13.46	0.52	22.56	0.80	**22.64**	**0.92**
	4	13.36	0.48	20.32	0.73	**21.23**	**0.85**
	5	13.72	0.48	**21.31**	0.76	19.45	**0.89**
Wedge	3	11.47	0.27	24.55	0.74	**26.23**	**0.92**
	4	10.66	0.24	18.05	0.61	**19.34**	**0.75**
	5	12.62	0.25	19.26	0.66	**20.13**	**0.80**

Number of Reference Spectra. To evaluate the capability of unmixing multiple spectra for XANES data, we generated two datasets at reference spectra ($L = 3, 4, 5$) when $\sigma = 3$. Here, different reference spectra represent different valence states of Ni, the phase map represents the proportions of different Ni valence states within the chemical material. The results of PSNRs and SSIMs are presented in Table 2, demonstrating our proposed framework's robustness and superiority. Note that RUM_{im} outperforms RUM_{ex} in most of the cases but the gap becomes smaller when there are more reference spectra. Additionally, Fig. 4 displays the phase maps of three reference spectra (Ni valence state 1, 2, 3, respectively.) using Wedge data, the three-phase maps respectively represent the proportions of state 1, 2, 3 within the Wedge, indicating that our phase maps are closer to GT. Furthermore, Fig. 5 shows the result with the number of reference spectra being 5 (Ni valence state 1, 2, 3, 4, 5, respectively), the five-phase maps respectively represent the proportions of state 1, 2, 3, 4 and 5 within the Particle. The phase maps with Particle data for Ni valence states 1, 2, and 5 obtained RUM method exhibit clearer structural details.
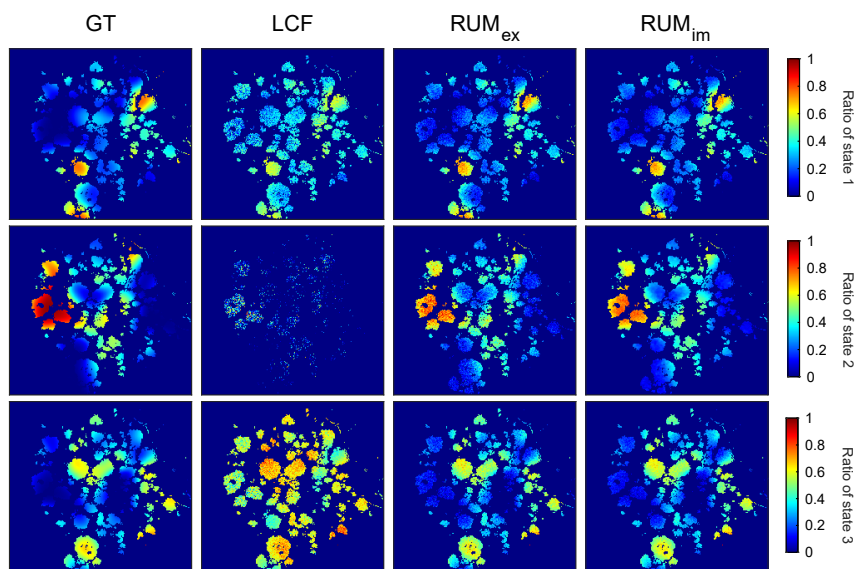
Fig. 4. The visual comparison for the chemical phase maps of the various methods on Wedge data under three reference spectra ($\sigma = 3$). From top to bottom: Ni valence state 1, 2, 3, respectively.

However, the structure of the phase map for Ni valence states 3 and 4 is unclear, suggesting a strong correlation between its reference spectra, and strongly correlated spectra may provide similar information, making it difficult to accurately distinguish between different components. Nevertheless, RUM$_{im}$ still outperforms other methods in unmixing multiple spectra.

The algorithm 1 framework is based on ADMM which decouples the forward model and the prior model terms in the optimization procedure. Mathematically, implicit regularization is designed to impose smoothness in the solution by penalizing the rate of change. In contrast, explicit regularization directly constrains the solution space, potentially leading to a more restrictive optimization landscape and may not accommodate the complexities of real-world data as effectively.

3.3. Results of Real Dataset

We apply the proposed RUM$_{ex}$ and RUM$_{im}$ methods to unmix real TXM-XANES data. The data comprises an image of numerous Nickel-Cobalt-Manganese (NCM) particles on a charged cathode, as shown on the left in Fig. 6. NCM particles were collected from 8180 eV to 8562 eV with varying energy intervals across the Ni K-edge, with spectral sampling of 0.5 eV in the immediate edge region. The zone plate was adjusted to maintain focus. NCM particles were recorded at each energy within 0.5 seconds of the sample image to account for changes in flux and small beam instabilities. The (fully automated) two-dimensional XANES measurement of a single field of view (FOV) can be accomplished within several minutes. Further time reduction can be achieved by limiting the number of energy points to the minimum necessary to discriminate different chemical phases, which, in turn, requires a priori knowledge of the chemical phases present in the sample. The two chemical phases present (different Ni states) were fit to XANES spectra of pure Ni.

The NCM particle data exhibits an extremely low signal-to-noise ratio, making it challenging to discern the reference spectra of Ni elements in the range of 8180 eV to 8562 eV under
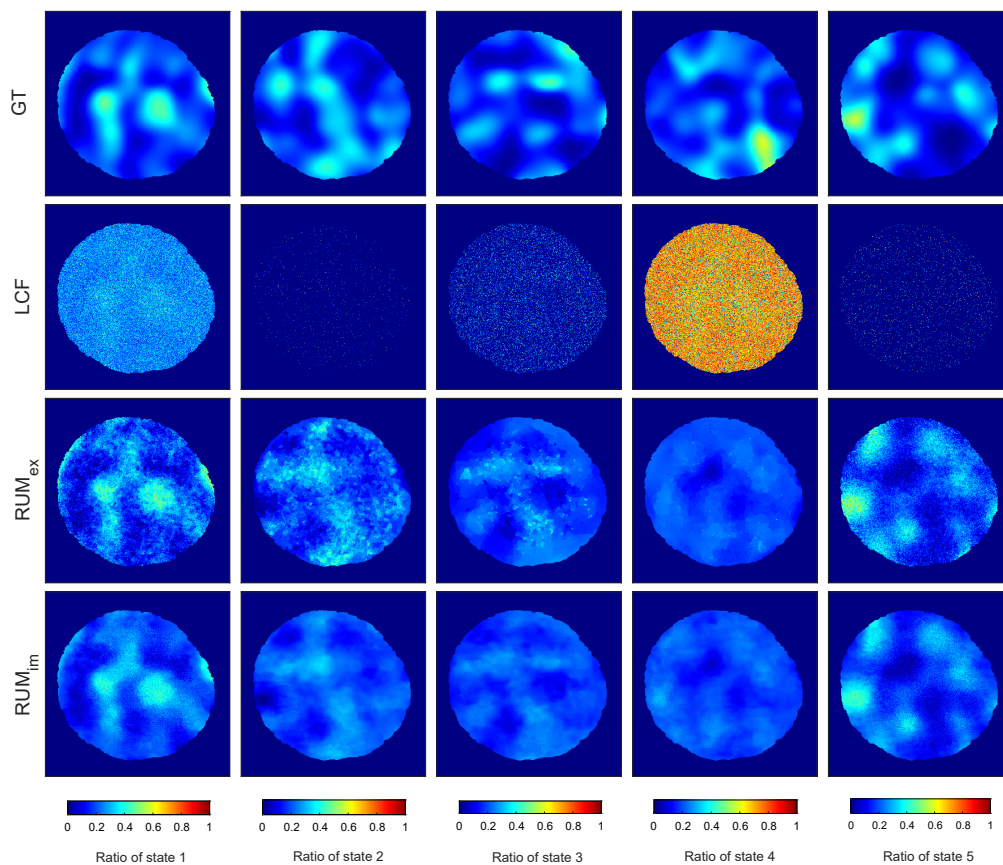
Fig. 5. The visual comparison for the chemical phase maps of the various methods on Particle data under five reference spectra ($\sigma = 3$). From left to right: Ni valence state 1, 2, 3, 4, 5, respectively.
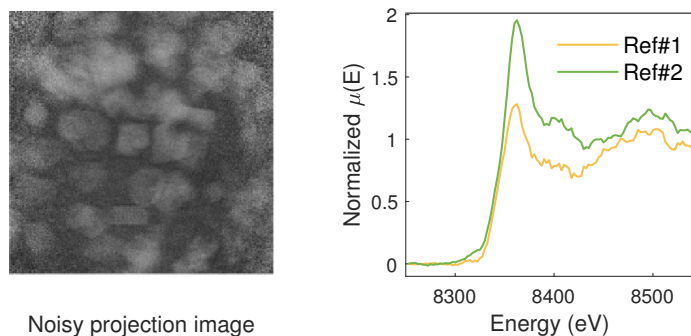

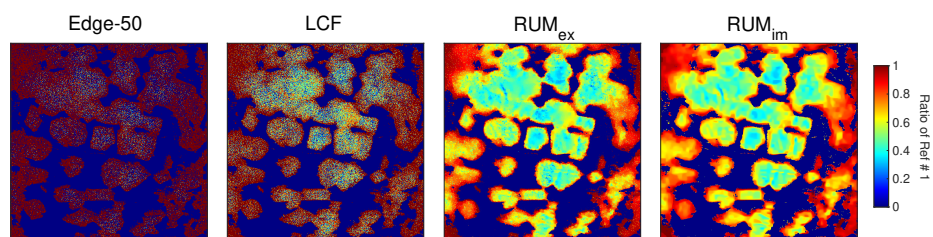Fig. 6. Low SNR projection image of TXM-XANES recording (left) and the reference spectra dictionary (right).

Fig. 7. The visual comparison for the chemical phase map of the various methods on NCM particle under two reference spectra (Ref#1 and Ref#2).

practical conditions. Consequently, we can only determine that it contains Ni at different internal states, similar to the blind unmixing. In order to tackle this challenge, we applied a denoising algorithm [16] to improve the projection images' signal-to-noise ratio (SNR). Following that, we employed the VCA algorithm [51] for dictionary extraction. Figure 6 on the right-hand side illustrates the two reference spectra for the two Ni states extracted by VCA [51] within the range of 8180 eV to 8562 eV. Despite the presence of noise in these extracted reference spectra, our method showcases resilience when working with noisy data. These techniques allowed us to overcome the low SNR and extract valuable information from the NCM particle data.

As shown in Fig. 7, the presented RUM algorithm adeptly discerns the relative proportions of the two Ni elements within the NCM particle structure. In real-world applications, it is customary to employ a linear transformation on the chemical maps that depict the proportions of these Ni elements. This transformation is guided by the absorption edge energies linked to the two reference spectra. The detailed chemical phase map is available in the Supplementary Material. Note that RUM_{ex} has some theoretical guarantee on the convergence while the RUM_{im} shows better unmixing results in the synthetic experiments. On the other hand, due to the high noise levels in each projection image of NCM particles, the chemical phase map obtained using Edge-50 and LCF fails to provide any meaningful information. Our methods simultaneously unmix and denoise the chemical imaging data, avoiding the accumulated error if we split these two processes. Additionally, the chemical phase map of NCM particles indicates an uneven reaction of the battery electrode, with some particles exhibiting a higher Ni valence state and others showing a lower Ni valence state. A major reason is that during the charge and discharge cycles of the battery, nickel ions undergo redox reactions and change between different Ni valence states [52, 53]. The utilization of the RUM unmixing method opens up avenues for enhanced understanding of spatiotemporally electrochemical reactions, enabling more profound insights and facilitating the optimization of composite electrode designs.

4. Conclusion

This paper introduced a robust spectra unmixing framework to extract the chemical phase map signal for the widely-used X-ray imaging technique. Our proposed framework considered variance in spectra and maximized the use of spatial-spectral priors in X-ray microspectroscopy. It outperforms traditional methods significantly when dealing with strong noise and spectral variability. Experimental results showcase substantial improvements when compared to traditional methods, with enhancements of up to 151.84% in PSNR and 136.33% in SSIM in simulated datasets. Additionally, the framework exhibits favorable convergence properties for the explicit regularization, while the implicit regularization performs better. Our future research involves extending the applicability of our model to scenarios with Poisson noise and practical applications where there is a strong correlation among reference spectral signatures. Another direction for our future work is to develop deep learning approaches by adapting the techniques in the 3D

chemical imaging reconstruction [54, 55]. Moreover, the denoising operator utilized in our proposed method is not limited to DnCNN. We have the flexibility to leverage more advanced denoising neural networks, including FFDNet [56] and Swin-transformer [57], to further elevate the unmixing performance for X-ray microspectroscopy.

Data Availability. Data underlying the results presented in this paper are not publicly available at this time but may be obtained from the authors upon reasonable request.

Supplemental document. See Supplement 1 for supporting content.

References

1. F. Meirer, J. Cabana, Y. Liu, A. Mehta, J. C. Andrews, and P. Pianetta, "Three-dimensional imaging of chemical phase transformations at the nanoscale with full-field transmission X-ray microscopy," J. Synchrotron Radiat. **18**, 773–781 (2011).
2. J. Wang, Y.-c. K. Chen-Wiegart, and J. Wang, "In operando tracking phase transformation evolution of lithium iron phosphate with hard X-ray microscopy," Nat. Commun. **5**, 4570 (2014).
3. U. Boesenberg, F. Meirer, Y. Liu, A. K. Shukla, R. Dell'Anna, T. Tyliszczak, G. Chen, J. C. Andrews, T. J. Richardson, R. Kostecki *et al.*, "Mesoscale phase distribution in single particles of LiFePO4 following lithium deintercalation," Chem. Mater. **25**, 1664–1672 (2013).
4. H. Yang, H.-H. Wu, M. Ge, L. Li, Y. Yuan, Q. Yao, J. Chen, L. Xia, J. Zheng, Z. Chen *et al.*, "Simultaneously dual modification of Ni-rich layered oxide cathode for high-energy lithium-ion batteries," Adv. Funct. Mater. **29**, 1808825 (2019).
5. K. Zhang, F. Ren, X. Wang, E. Hu, Y. Xu, X.-Q. Yang, H. Li, L. Chen, P. Pianetta, A. Mehta *et al.*, "Finding a needle in the haystack: identification of functionally important minority phases in an operating battery," Nano Lett. **17**, 7782–7788 (2017).
6. Y. Xu, E. Hu, K. Zhang, X. Wang, V. Borzenets, Z. Sun, P. Pianetta, X. Yu, Y. Liu, X.-Q. Yang *et al.*, "In situ visualization of state-of-charge heterogeneity within a LiCoO2 particle that evolves upon cycling at different rates," ACS Energy Lett. **2**, 1240–1245 (2017).
7. Z. Jiang, J. Li, Y. Yang, L. Mu, C. Wei, X. Yu, P. Pianetta, K. Zhao, P. Cloetens, F. Lin *et al.*, "Machine-learning-revealed statistics of the particle-carbon/binder detachment in lithium-ion battery cathodes," Nat. Commun. **11**, 2310 (2020).
8. G. Qian, J. Zhang, S.-Q. Chu, J. Li, K. Zhang, Q. Yuan, Z.-F. Ma, P. Pianetta, L. Li, K. Jung *et al.*, "Understanding the mesoscale degradation in nickel-rich cathode materials through machine-learning-revealed strain–redox decoupling," ACS Energy Lett. **6**, 687–693 (2021).
9. G. J. Nelson, W. M. Harris, J. R. Izzo Jr, K. N. Grew, W. K. Chiu, Y. S. Chu, J. Yi, J. C. Andrews, Y. Liu, and P. Pianetta, "Three-dimensional mapping of nickel oxidation states using full field X-ray absorption near edge structure nanotomography," Appl. Phys. Lett. **98**, 173109 (2011).
10. M. Newville, "Fundamentals of XAFS," Rev. Mineral. Geochem. **78**, 33–74 (2014).
11. J. Prietzel, A. Botzaki, N. Tyufekchieva, M. Brettholle, J. Thieme, and W. Klysubun, "Sulfur speciation in soil by SK-edge XANES spectroscopy: comparison of spectral deconvolution and linear combination fitting," Environ. Sci. & Technol. **45**, 2878–2886 (2011).
12. J. P. Gustafsson, S. Braun, J. M. Tuyishime, G. A. Adediran, R. Warrinnier, and D. Hesterberg, "A probabilistic approach to phosphorus speciation of soils using P K-edge XANES spectroscopy with linear combination fitting," Soil Syst. **4**, 26 (2020).
13. D. Hesterberg, I. McNulty, and J. Thieme, "Speciation of soil phosphorus assessed by XANES spectroscopy at different spatial scales," J. Environ. Qual. **46**, 1190–1197 (2017).
14. M. Tabuchi, R. Sakamoto, S. Takeda, S. Konishi, T. Suzuki, and T. Nagami, "Modified linear combination fitting for large-area two-dimensional chemical state mapping," Radiat. Phys. Chem. **175**, 108257 (2020).
15. X. Xiao, Z. Xu, F. Lin, and W.-K. Lee, "Txm-sandbox: an open-source software for transmission x-ray microscopy data analysis," J. Synchrotron Radiat. **29**, 266–275 (2022).
16. J. Li, B. Chen, G. Zan, G. Qian, P. Pianetta, and Y. Liu, "Subspace modeling enabled high-sensitivity X-ray chemical imaging," in *ICASSP 2023 - 2023 IEEE International Conference on Acoustics, Speech and Signal Processing (ICASSP),* (2023), pp. 1–5.
17. B. A. Anzures, S. W. Parman, R. E. Milliken, A. Lanzirotti, and M. Newville, "XANES spectroscopy of sulfides stable under reducing conditions," Am. Mineral. J. Earth Planet. Mater. **105**, 375–381 (2020).
18. N. Keshava and J. F. Mustard, "Spectral unmixing," IEEE Signal Process. Mag. **19**, 44–57 (2002).

19. W.-K. Ma, J. M. Bioucas-Dias, T.-H. Chan, N. Gillis, P. Gader, A. J. Plaza, A. Ambikapathi, and C.-Y. Chi, "A signal processing perspective on hyperspectral unmixing: Insights from remote sensing," IEEE Signal Process. Mag. **31**, 67–81 (2013).

20. H. Li, R. Feng, L. Wang, Y. Zhong, and L. Zhang, "Superpixel-based reweighted low-rank and total variation sparse unmixing for hyperspectral remote sensing imagery," IEEE Transactions on Geosci. Remote. Sens. **59**, 629–647 (2020).

21. Z. Wang, J. Li, Y. Liu, F. Xie, and P. Li, "An adaptive surrogate-assisted endmember extraction framework based on intelligent optimization algorithms for hyperspectral remote sensing images," Remote. Sens. **14**, 892 (2022).

22. S. Tzoumas and V. Ntziachristos, "Spectral unmixing techniques for optoacoustic imaging of tissue pathophysiology," Philos. Transactions Royal Soc. A: Math. Phys. Eng. Sci. **375**, 20170262 (2017).

23. B. Ayhan, C. Kwan, and S. Vance, "On the use of a linear spectral unmixing technique for concentration estimation of APXS spectrum," J. Multidiscip. Eng. Sci. Technol. **2**, 2469–2474 (2015).

24. T. YangDai and L. Zhang, "Spectral unmixing method for multi-pixel energy dispersive X-ray diffraction systems," Appl. Opt. **56**, 907–915 (2017).

25. D. Rossouw, P. Burdet, F. de la Peña, C. Ducati, B. R. Knappett, A. E. Wheatley, and P. A. Midgley, "Multicomponent signal unmixing from nanoheterostructures: Overcoming the traditional challenges of nanoscale x-ray analysis via machine learning," Nano Lett. **15**, 2716–2720 (2015).

26. R. Heylen, M. Parente, and P. Gader, "A review of nonlinear hyperspectral unmixing methods," IEEE J. Sel. Top. Appl. Earth Obs. Remote. Sens. **7**, 1844–1868 (2014).

27. J. M. Bioucas-Dias, A. Plaza, N. Dobigeon, M. Parente, Q. Du, P. Gader, and J. Chanussot, "Hyperspectral unmixing overview: Geometrical, statistical, and sparse regression-based approaches," IEEE J. Sel. Top. Appl. Earth Obs. Remote. Sens. **5**, 354–379 (2012).

28. L. Drumetz, M.-A. Veganzones, S. Henrot, R. Phlypo, J. Chanussot, and C. Jutten, "Blind hyperspectral unmixing using an extended linear mixing model to address spectral variability," IEEE Transactions on Image Process. **25**, 3890–3905 (2016).

29. D. Hong, N. Yokoya, J. Chanussot, and X. X. Zhu, "An augmented linear mixing model to address spectral variability for hyperspectral unmixing," IEEE Transactions on Image Process. **28**, 1923–1938 (2018).

30. R. A. Borsoi, T. Imbiriba, J. C. M. Bermudez, C. Richard, J. Chanussot, L. Drumetz, J.-Y. Tourneret, A. Zare, and C. Jutten, "Spectral variability in hyperspectral data unmixing: A comprehensive review," IEEE Geosci. Remote. Sens. Mag. **9**, 223–270 (2021).

31. L. Drumetz, J. Chanussot, C. Jutten, W.-K. Ma, and A. Iwasaki, "Spectral variability aware blind hyperspectral image unmixing based on convex geometry," IEEE Transactions on Image Process. **29**, 4568–4582 (2020).

32. S. G. Azar, S. Meshgini, S. Beheshti, and T. Y. Rezaii, "Linear mixing model with scaled bundle dictionary for hyperspectral unmixing with spectral variability," Signal Process. **188**, 108214 (2021).

33. M.-D. Iordache, J. M. Bioucas-Dias, and A. Plaza, "Total variation spatial regularization for sparse hyperspectral unmixing," IEEE Transactions on Geosci. Remote. Sens. **50**, 4484–4502 (2012).

34. I. A. Cruz-Guerrero, D. U. Campos-Delgado, and A. R. Mejía-Rodríguez, "Extended blind endmember and abundance estimation with spatial total variation for hyperspectral imaging," in *2021 43rd Annual International Conference of the IEEE Engineering in Medicine & Biology Society (EMBC),* (2021), pp. 1957–1960.

35. B. Lin, X. Tao, and J. Lu, "Hyperspectral image denoising via matrix factorization and deep prior regularization," IEEE Transactions on Image Process. **29**, 565–578 (2019).

36. D. Gong, Z. Zhang, Q. Shi, A. van den Hengel, C. Shen, and Y. Zhang, "Learning deep gradient descent optimization for image deconvolution," IEEE Transactions on Neural Networks Learn. Syst. **31**, 5468–5482 (2020).

37. X. Wang, J. Chen, C. Richard, and D. Brie, "Learning spectral-spatial prior via 3DDNCNN for hyperspectral image deconvolution," in *ICASSP 2020-2020 IEEE International Conference on Acoustics, Speech and Signal Processing (ICASSP),* (2020), pp. 2403–2407.

38. M. Zhao, X. Wang, J. Chen, and W. Chen, "A plug-and-play priors framework for hyperspectral unmixing," IEEE Transactions on Geosci. Remote. Sens. **60**, 1–13 (2021).

39. J. Chen, M. Zhao, X. Wang, C. Richard, and S. Rahardja, "Integration of physics-based and data-driven models for hyperspectral image unmixing: A summary of current methods," IEEE Signal Process. Mag. **40**, 61–74 (2023).

40. X. Chang, L. Bian, and J. Zhang, "Large-scale phase retrieval," eLight **1**, 1–12 (2021).

41. X. Chang, L. Bian, Y. Gao, L. Cao, J. Suo, and J. Zhang, "Plug-and-play pixel super-resolution phase retrieval for digital holography," Opt. Lett. **47**, 2658–2661 (2022).

42. W. Meiniel, J.-C. Olivo-Marin, and E. D. Angelini, "Denoising of microscopy images: a review of the state-of-the-art, and a new sparsity-based method," IEEE Transactions on Image Process. **27**, 3842–3856 (2018).

43. J. Peng, W. Sun, H.-C. Li, W. Li, X. Meng, C. Ge, and Q. Du, "Low-rank and sparse representation for hyperspectral image processing: A review," IEEE Geosci. Remote. Sens. Mag. **10**, 10–43 (2021).

44. L. I. Rudin, S. Osher, and E. Fatemi, "Nonlinear total variation based noise removal algorithms," Phys. D: nonlinear phenomena **60**, 259–268 (1992).

45. S. Boyd, N. Parikh, E. Chu, B. Peleato, J. Eckstein *et al.*, "Distributed optimization and statistical learning via the alternating direction method of multipliers," Foundations Trends Mach. learning **3**, 1–122 (2011).

46. W. L. Winston, *Operations research: applications and algorithm* (Thomson Learning, Inc., 2004).

47. K. Dabov, A. Foi, V. Katkovnik, and K. Egiazarian, "Image denoising by sparse 3-D transform-domain collaborative

437   filtering," IEEE Transactions on Image Process. **16**, 2080–2095 (2007).

48. K. Zhang, W. Zuo, Y. Chen, D. Meng, and L. Zhang, "Beyond a gaussian denoiser: Residual learning of deep cnn for image denoising," IEEE Transactions on Image Process. **26**, 3142–3155 (2017).

49. Z. T. Harmany, R. F. Marcia, and R. M. Willett, "This is SPIRAL-TAP: Sparse Poisson intensity reconstruction algorithms—theory and practice," IEEE Transactions on Image Process. **21**, 1084–1096 (2011).

50. Y. Wang, J. Yang, W. Yin, and Y. Zhang, "A new alternating minimization algorithm for total variation image reconstruction," SIAM J. on Imaging Sci. **1**, 248–272 (2008).

51. J. M. Nascimento and J. M. Dias, "Vertex component analysis: A fast algorithm to unmix hyperspectral data," IEEE Transactions on Geosci. Remote. Sens. **43**, 898–910 (2005).

52. M. Dixit, B. Markovsky, F. Schipper, D. Aurbach, and D. T. Major, "Origin of structural degradation during cycling and low thermal stability of Ni-rich layered transition metal-based electrode materials," The journal physical chemistry C **121**, 22628–22636 (2017).

53. L. S. de Vasconcelos, R. Xu, Z. Xu, J. Zhang, N. Sharma, S. R. Shah, J. Han, X. He, X. Wu, H. Sun *et al.*, "Chemomechanics of rechargeable batteries: status, theories, and perspectives," Chem. Rev. **122**, 13043–13107 (2022).

54. Y. Huang, S. Wang, Y. Guan, and A. Maier, "Limited angle tomography for transmission X-ray microscopy using deep learning," J. Synchrotron Radiat. **27**, 477–485 (2020).

55. H. Villarraga-Gómez, M. N. Rad, M. Andrew, A. Andreyev, R. Sanapala, L. Omlor, and C. G. vom Hagen, "Improving throughput and image quality of high-resolution 3D X-ray microscopes using deep learning reconstruction techniques," in *11th Conference on Industrial Computed Tomography (iCT),* (2022), pp. 8–11.

56. K. Zhang, W. Zuo, and L. Zhang, "FFDNet: Toward a fast and flexible solution for CNN-based image denoising," IEEE Transactions on Image Process. **27**, 4608–4622.

57. K. Zhang, Y. Li, J. Liang, J. Cao, Y. Zhang, H. Tang, D.-P. Fan, R. Timofte, and L. V. Gool, "Practical blind image denoising via Swin-Conv-UNet and data dynthesis," Mach. Intell. Res. pp. 1–14 (2023).